# Understanding the Long-term Tidal Modulation on Methane Bubble Emissions at Southern Hydrate Ridge using Acoustics

Bing Yu Lee

University of Washington, Seattle, WA

School of Oceanography, Box 357940

bingyu@uw.edu

June 2nd, 2019

## 1. ABSTRACT

Methane release from seafloor reservoirs is thought to have caused paleo-climate warming and have the potential to accelerate global warming. Methane reservoirs along the upper continental slope are especially susceptible to destabilization due to the narrow margin of hydrate stability within the seafloor. At Southern Hydrate Ridge (SHR), discontinuity in methane bubble emissions was observed, but still not well understood. Our study uses acoustic data archived by the Ocean Observatories Initiative (OOI) Cabled Array to investigate the potential tidal impact on methane bubble emissions at SHR. We detect methane plume structures based on the proxy of echo contrasts caused by acoustic-bubble interaction. Through analyzing the cumulative frequency of methane bubble emissions over a tidal cycle, we deduce a sinusoidal bubble plume response curve with ~120-degree lag from a cosine curve of tidal forcing. Our result reveals significant tidal modulation on bubble emissions with an abundance difference up to ~2.5 times over ~3.5 months. During the phase of falling tides, frequency of methane emissions is higher. Tidally induced pressure change could modulate the pore fluid pressure system by promoting or inhibiting fracturing that could cause bubble emissions. We propose a model for the dynamic equilibrium between the seafloor pressure and the pore fluid pressure for SHR. Our study has demonstrated the application of high-temporal resolution Acoustic Doppler Current Profiler (ADCP) in studying methane bubbles.

## 2. ACKNOWLEDGEMENT

Firstly, I would like to express my sincere gratitude to my advisors Prof. Delaney, Prof. Hautala and Brendan Philip of the School of Oceanography at the University of Washington. Their guidance, patience, motivation, technical assistance and science advice throughout the 9-month research have made this study possible. Thank you!

Besides my advisors, I am grateful to Ocean Observatories Initiative funded by the National Science Foundation for the data access to conduct the study. Special thanks to the UW VISIONS' 18 at-sea program (led by Prof. Kelley) which provided my first direct view of SHR and an introduction to this seep site. Many thanks to Mary Gates Endowment for Students for providing funding support.

Nevertheless, I would like to thank our senior thesis instructor Prof. Nowell and my fellow classmates for their encouragement, comments and support throughout the study. I am also grateful to experts who had given me advice throughout the research project: Prof. Deborah Kelley, Prof. William Wilcock, Prof. Paul Johnson, Orest Kawka, Kellen Rosburg, Erik Fredrickson, Emma Myers and Rose Ward. Last but not least, heartfelt thanks goes to my friends and family for their emotional support throughout the study.

## 3. INTRODUCTION

Methane hydrate has gained global attention for both its potential as an energy resource and the potential to drive climate change. Hence, scientific research related to methane hydrate has been conducted in 82 countries around the world (Liu et al., 2019). The worldwide distribution of methane hydrate and the compound's high energy density of gas volume ~164 times that of methane gas have made methane hydrate known to be a promising energy resource before the carbon-free age (Beaudoin et al., 2014; Liu et al., 2019). On the other hand, hydrate degassing, which releases methane into the hydrosphere and atmosphere, could exacerbate global warming and cause marine extinction (Archer, 2007; Bralower and Bice, n.d; Johnson et al. 2015; Katz et al., 2001; Liu et al., 2019).

Methane hydrate is an ice-like compound that forms as methane and water combine under low-temperature and high pressure, in which methane is concentrated within the molecular framework of a frozen water molecule (Ruppel, 2011; Solomon et al., 2008). As the most prevalent kind of gas hydrate (~99%) found worldwide (Liu et al., 2019), methane hydrate can only form within the methane hydrate stability zone (MHSZ) (Figure 1) limited by the ideal temperature and pressure for its formation (Ruppel, 2011). As a result, more than 99% of the global inventory of methane hydrate occurs in the marine continental margins with high organic content (Liu et al., 2019).

Methane hydrate located at the upper continental slope margin is highly susceptible to dissociation. In this geological setting, MHSZ is very close to the seafloor (Ruppel, 2011). Specifically, dissociation of methane hydrate could be easily triggered by either an increase in the seafloor temperature due to warming (Johnson et al. 2015), or disruption of the seafloor

stress system due to slope failure, erosion, earthquakes (Katz et al., 2001) and tides (Römer et al., 2016; Torres et al., 2002; Tyron et al., 1999). When methane hydrate dissociates, methane gas can dissolve in local pore waters, be trapped within the sediments or be delivered to the shallow ocean and atmosphere as bubbles (McGinnis et al., 2006).

Methane release from methane hydrate reservoirs can play an important role in global warming and marine extinction. During the Paleocene-Eocene Thermal Maximum (PETM), the increase in bottom water temperature and underwater slope failures may have caused chronic and catastrophic methane release from these reservoirs (Archer, 2007; Bralower and Bice, n.d). In congruence with the massive influx of methane into the hydrosphere and atmosphere, paleoclimate records have revealed temperature increase of 4 to 6 $^{o}$C in the deep sea and high latitude surface water (Katz et al., 2001). Following the warming ocean, archaic mammal and many deep-sea species went extinct. In addition, the coupled anoxia and decreased pH in the near-bottom water had led to the disappearance of ~55% of the foraminiferal taxa during the PETM (Johnson et al. 2015; Katz et al., 2001). Such disappearance of species due to climate warming marks the PETM the greatest deep-sea mass extinction in the last 93 Myr (Bralower and Bice, n.d).

Because methane is a very powerful greenhouse gas with a potency over 70 times that of carbon dioxide's over 20 years (Liu et al., 2019), its discovery in the form of hydrates underlying marine sediments at the continental slope margin has recently raised concerns among scientists. Destabilization of these hydrate compounds by global warming or slope failure associated with earthquakes could lead to massive release of methane into the ocean and atmosphere, further accelerating global warming (Johnson et al. 2015; Katz et al., 2001). Although our abilities to

detect and recover methane hydrate has flourished in the last decade (Beaudoin et al., 2014; Liu et al., 2019; National Research Council, 2010), and a lot of studies had been done to determine the global methane flux into the ocean, the exact contribution of methane seeps to the global ocean carbon budget is still poorly constrained. This is mainly due to our poor understanding of the complex gas-hydrate derived methane seepage system (Liu et al., 2019) and the discontinuous spatial and temporal distributions of methane seepage around the world (Johnson et al. 2015; Riedel et. al., 2018). Therefore, our study aims to understand the temporal variability of methane bubble seepage through investigating an active seep site located on an upper continental slope margin in the northeastern Pacific offshore of the North American plate — Southern Hydrate Ridge.

Located ~90 km offshore of the Newport, Oregon (Figure 2) at ~800 m depth, SHR is an extensively studied site under the National Science Foundation's Ocean Observatory Initiative (OOI) cabled array. Sitting along the Cascadia subduction margin, SHR was formed from organic-rich sediments on the subducting oceanic plate that were scraped off, folded and faulted into this accretionary ridge (Geologic History, n.d.). As the organic materials in the sediments are utilized by methanotrophic microbes resulting in methane saturation within the sediment pores, methane hydrate can form within the MHSZ (Geologic History, n.d.; Riedel et. al., 2018). At SHR, the base of MHSZ is located at ~120-150 m below seafloor (Bangs, Musgrave and Trehu, 2005).

Methane bubble emissions at the SHR are hypothesized to be controlled by the local hydraulic fracturing system (Daigle, Bangs and Dugan, 2011). Underlying the seafloor sediments at the depth of ~15-20 m below the base of MHSZ,  2-4-m-thick coarse-grained turbidites have

been found acting as permeable conduits that allow methane gas to be supplied to the shallow seafloor. Within the porous medium of the seafloor sediments below the base of MHSZ, methane gas is trapped due to reduced permeability near the seafloor resulting from hydrate-filled fractures. As methane gas accumulates following methane hydrate dissociation near the base of MHSZ, pore pressure builds up within the sediment. When pore pressure exceeds the effective overlying stress exerted by the overlying sediments and water column, fractures would form allowing the methane bubbles to escape into the ocean.

Although some studies have suggested the potential tidal influence on methane bubble emissions (Torres et al., 2002; Tyron et al., 1999), bubble emissions behavior at SHR is still not well understood — there is no statistical correlation found yet between tides and bubble emissions. Previous studies have found the bubble emissions behavior at SHR to be transient and episodic (Philip et al., 2016; Riedel et. al., 2018). On the other hand, a recent study at the Clayoquot Slope offshore of British Columbia suggested that falling tides (reducing water load/ pressure) could shift the hydrate solubility and induce bubble emissions (Römer et al., 2016). Therefore, to understand the temporal variability of methane bubble emissions at SHR, our study investigates the potential tidal impact on methane bubble emissions. Our study uses OOI acoustic data at SHR to test the hypothesis that tides have controls over methane bubble emissions such that falling tides could induce bubble emissions.

## 4. METHOD

To analyze the long-term variability of methane bubble emissions at SHR, we infer the presence of methane bubbles using acoustic contrast signals reflected in the ADCP's echo intensity. Such an application has been presented in previous studies to detect methane bubbles (Philip et al., 2016; Wiggins et al., 2015). Because a bubble has much a lower density than the surrounding seawater, the bubble-seawater interface has high impedance contrast. As a result, an ADCP would record high signal intensities of echos returning from the bubbles when they intersect the ADCP beams (Figure 4). The data acquisition, processing and analysis workflow for our study are summarized in Figure 3.

### 4.1 ADCP Monitoring

At SHR, a four-beam Teledyne RD Instruments (TRDI) Workhorse Longranger 75-kHz ADCP was deployed on the OOI Regional Cabled Array on September 18$^{th}$, 2014. On the basis of Doppler frequency shift from the returning pulses reflected off moving water particles, the ADCP transmits acoustic pulses at an interval of 2.5s to measure the current velocities throughout the water column. All four of the ADCP beams are angled at 20$^{o}$ from vertical (Figure 4), passing overhead of several well-documented active seep sites, Seep B and Einstein's Grotto, in the region (Figure 5). Each ensemble of measurements has a vertical resolution of 8-m depth with minimum measured height above the seafloor at 16.73m.

### 4.2 Data Acquisition & Processing

We acquired echo intensity and current velocity data from the ADCP, and seafloor pressure data from the bottom pressure recorder (BPR). These data are archived in the OOI data portal (OOI,

2018). Due to our 9-month time constraint for the study, we analyzed the data for the time period of about 3.5 months from March 3rd to June 23rd, 2015 as opposed to the 4-5 years archived data.

From the raw ADCP data file, we calculated the horizontal current velocities and their corresponding depths. Using the transformation matrix and the rotation matrix described in the OOI data product specification (2012), we converted the ADCP data from its binary form of beam coordinates to Earth's coordinates to calculate the horizontal current velocities. By taking into account of the beams' configuration and the local magnetic declination during the study period, our calculation includes corrections of heading, pitch, roll angle and magnetic variation for the instrument. For the magnetic variance correction, we use a declination angle of 15.7573° averaged from World Magnetic Model and International Geomagnetic Reference Field over the study period. Depth values corresponding to the ADCP data were calculated using the known value of bin-cell-length and minimum measured height above the seafloor.

To amplify the acoustic contrast signals, we cleaned the echo intensity data through the removal of background intensities and threshold filtering. We subtracted background intensities from our data using the 3-hour-averaged background intensities derived when methane bubble plumes were absent. After that, we filtered the data with a selected threshold intensity of 23 dB to eliminate most of the noise in our data while preserving the acoustic contrast signals. The source of some of these "noise" includes bodies of sediments and planktons (zooplankton, fishes) in the water. The cleaned cross section of echo intensities is then used for our data analysis (Figure 6A).

### 4.3 Data Analysis

We averaged the horizontal velocities over the depth range of 80 m above the seafloor on an hourly and weekly basis. Using the weekly-averaged velocities, we calculated the local weekly-average prevailing background current speed and direction (Figure 7A). On the basis of the hourly-averaged velocities, we calculated the local average tidal current speed and direction (Figure 7B). From the cleaned cross section of echo intensities, we counted the number of bin cells with the presence of methane bubbles throughout our study period. We further applied 2-standard-deviation cleaning on the counted presence, which gives rise to 95% confidence level of bubble detection, to completely eliminate false detection that could be resulted from the remaining noise (Figure 6B). To analyze all data sets over the same time scale, we reconstruct the pressure data within the time range of ADCP data using the linear interpolation tool on MATLAB. For our analysis, we combined the bubble detections from all beams. We then plotted the prevailing background current speed and direction, tidal current speed and direction, seafloor pressure, and the counted presence of methane bubbles over the same time axis (Figure 7).

To evaluate the detection of methane bubbles by the ADCP, we analyzed the distribution of flow directions of the detected methane bubbles in individual ADCP beam using the local tidal current direction derived from the tidal current velocities (Figure 8). We also analyzed the distribution of local current speed (Figure 9A) to identify the potential bubble source locations. Assuming a general bubble rising velocity, $V_{bubble}$, of 30 cm/s (Rehder et al., 2009) and a maximum bubble rise height of 350 m (Figure 10), we calculated the methane bubble source distances and the bubble rising angles from vertical based on the ADCP beam geometry. We then

evaluated the potential bubble source locations based on the distribution of the potential methane bubble source distances (Figure 9B) and the bubble rising angles (Figure 9C).

To study the long-term impact of tidal action on methane bubble emissions, we segmented the counted presence of methane bubbles based on a tidal cycle from high tide to high tide, with each tidal cycle represented by $360^{o}$, in similar to that of a cosine wave function. Then, we summed the number of detections of methane bubbles that occurred in the same phase of tidal cycles throughout our study period. As discussed in more detail in the results section, we concluded that during periods of NW-flowing prevailing background current and N-NW-dominated tidal current, bubble plumes tended to not intersect the ADCP beams (Figure 7). Thus, we excluded the data sets within these periods from our analysis to prevent any bias in our result. Finally, we plotted the cumulative detections over with the tidal cycle (Figure 11). We then perform t-test on the peak and trough phases of cumulative detections to determine the confidence intervals of maximum and minimum cumulative detections. By comparing the lower bound of maximum detections and upper bound of minimum detections, we examine the statistical significance of the tidal impact on methane bubble emissions over the study period.

## 5. RESULTS

Our data reveals detection of methane bubble plumes throughout the tidal cycle (Figure 11B). Throughout our study period, the maximum seafloor pressure change due to tides is ~3.3 dbar approximating ~3.3 meter change in water depth. Our cumulative methane bubble detections over the tidal cycle exhibit a sinusoidal behavior with a phase lag of ~120 degree between high tides (Figure 11A) and the highest abundance of bubble plume detections (Figure 11B). The highest number of detections occurs as tides progressed from high tide to low tide. Contrariwise, as tides progressed from low tide to high tide, we found significantly lower number of detections. Comparing the lower bound of detection peak to upper bound of detection trough, we deduced a detection peak to trough ratio of ~2.5.

Methane bubbles were detected in all four beams of the ADCP (Figure 7C). We observed significant reductions in the detection of methane bubble plumes (Figure 7C) during time period dominated by northwestward prevailing background current (Figure 7A) with tidal current directions fluctuates mostly between N-NW (Figure 7B). From the distribution of flow direction of the detected methane bubbles, which depends on the tidal current, in the individual ADCP beam (Figure 8), we found that the methane bubbles detected in beam 1 were predominantly flowing southeast and northeast. Those detected in beam 2 were predominantly flowing southwest and northwest. On the other hand, methane bubbles detected in beam 3 were predominantly flowing north, northeast and northwest. Lastly, those detected in beam 4 were predominantly flowing southwest, south and southeast.

As a result of our 2-standard-deviation cleaning on the counted presence, the lower limits of methane presence are 10 bins for beam 1, 11 bins for beam 2 and beam 4, and 12 bins for

beam 3. On the other hand, we found the upper limits of methane presence to be 44 bins for beam 1, 37 bins for beam 2, 42 bins for beam 3 and beam 4. Translating the upper-limit bins of methane presence into depth, we found that methane bubbles rise to a maximum height of ~350 m above the seafloor (~ 400 m below sea surface) (Figure 10).

Analyzing the distribution of the local tidal current speed, we found a mean tidal current speed of ~9.3 cm/s with a standard deviation of ~3.7 cm/s (Figure 9A). On the other hand, our calculation of methane bubble source distances indicates a mean distance of ~100 m with a standard deviation of ~44 m (Figure 9B). Analyzing the trigonometric relationship between the tidal current speed and $V_{bubble}$, we found a mean bubble rising angle from vertical of 15.74$^{o}$ with a standard deviation of 6.59$^{o}$ (Figure 9C).

## 6. DISCUSSION

### 6.1 Long-term tidal modulation on methane bubble emissions

Our result suggests a modification to the hypothesis in the case of SHR. Instead of inducing bubble emissions, our result reveals how tides could modulate the abundance of bubble plumes over the long-term, 3.5 months in this case, with an abundance difference up to ~2.5 times (Figure 11). Unlike the case in Clayoquot Slope offshore of British Columbia (Römer et al., 2016), bubble emissions at SHR were significantly detected throughout the tidal phase over the 3.5-month observation (Figure 7, Figure 11).

This tidally-modulated bubble emissions behavior further indicates that the underlying pore fluid pressure system at SHR is most likely a dynamic pressure system such that the pore fluid pressure system at the base of MHSZ may behave independently from the hydrostatic pressure system (seafloor pressure system). Assuming a hydraulic fracturing system (Daigle, Bangs and Dugan, 2011) at SHR, bubble emissions occur when fracture forms or reopens as a result of pore pressure from bubble build-up overcoming the effective overlying stress. At the phase of falling tides, decreasing seafloor pressure, meaning that the effective overlying stress is reducing, would facilitate the bubble flux by reopening the pre-existing fractures (Römer et al., 2016). If the pore fluid pressure system was passive, meaning that the pore fluid pressure is dependent on the hydrostatic pressure, we expect bubble emission behavior similar to that observed at Clayoquot Slope. However, because there is a ~120-degree lag between the nearly sinusoidal tidal forcing and bubble plume response curves (Figure 11), we suggest that SHR may have a dynamic pore fluid pressure system as opposed to the passive system found in Clayoquot Slope (Römer et al., 2016).

With that, we present a conceptual model with a cycle of 4 phases of bubble emissions (Figure 12) assuming a hydraulic fracturing system (Daigle, Bangs and Dugan, 2011) with continuous fueling of gas bubbles below the MHSZ. If sediment pore pressure is low during the phase of high tide (high seafloor pressure), there is a low tendency of the effective overlying stress overcome by pore pressure, therefore bubble emissions are less likely (Phase 1). As bubble pressure builds up within the sediment, the frequency of bubble emissions increases. However, due to the inhibition from high seafloor pressure, bubble emissions frequency is limited to a moderate level (Phase 2). The highest frequency of bubble emissions occurs when tidal pressure decreases (Phase 3). When pore pressure drops because of the greater bubble flux into the water column, bubble emissions frequency reduces again to a moderate level (Phase 4). The cycle starts over again when tidal pressure increases, inhibiting bubble flux from the seafloor.

### 6.2 Bubble sources

Our results of the ADCP detections, tidal current speed and bubble rising angles suggest close-proximity bubble sources. Analyzing the distribution of the local tidal current speed, we found that the tidal current speed is below 16.76 cm/s 95% of the time during our study period (Figure 9A). Comparing $V_{bubble}$ to the tidal current speed, our result indicates a typical $V_{bubble}$ to tidal current speed ratio of ~1.8. This poses a limitation in terms of the maximum source distances for the detected bubbles. Our analysis indicates that 95% of the detected bubbles have source distances within ~188 m (Figure 9B) and bubble-rising angles smaller than 28.92$^{o}$ (Figure 9C). Coupling these values with the relatively lower mean distance of 100.05 m and lower mean angle of 15.74$^{o}$, we argue that the sources of detected bubbles are close to the ADCP. For the ADCP to

detect bubbles from more distant sources, horizontal tidal current with high speed (low $V_{bubble}$ to current speed ratio) is necessary.

The relationship between the beam detections and the directions of tidal current (Figure 8) indicates that most of the detections of methane bubble presence are most likely contributed by the two previously documented active seep sites: Seep B and Einstein's Grotto. If methane bubbles do come from these seep sites, the bubbles would follow the flow direction away from the seep sites. Our observation indicates a trend that most of the detected bubbles have flow directions pointing away from the ADCP and these seep sites (solid arrows in Figure 8B). However, out of the 10 predominant flow directions of detected bubbles, 2 of them (dashed arrow in Figure 8B) disobey the trend — though still pointing away from the ADCP, they are not parallel to the directions away from any of these seep sites. Two reasons could explain these detection anomalies: (1) there could be another active bubble source south of the ADCP, and, (2) the bubble plume may have bent due to inconsistent current directions along the vertical profile of the water column. Inconsistency in the current directions along the vertical profile of the water column could be contributed by the tidally induced change in current direction (Figure 7B) or the intermediate nepheloid layers. At SHR, nepheloid layers resulting from the California undercurrent has been observed transporting methane offshore (Heeschen et al., 2005). To determine the exact cause of these detection anomalies, a high-resolution analysis on current speed and bubble presence along the vertical profile is necessary. If bubble plumes are present consistently throughout the vertical profile from a low height (such as the plume highlighted in the red box in Figure 10), the former reason is likely the cause of the anomalies. Otherwise, if bubble plumes are only present in the detection beam at mid-height (such as the plume

highlighted in the green box in Figure 10), the latter reason is likely the cause. Although some of the detections in our study show inconsistency with the trend in which the detected bubbles have flow directions pointing away from the ADCP and the seep sites, our overall data analysis suggests that Seep B and Einstein's Grotto are most likely the major bubble sources.

### 6.3 ADCP detection evaluation

Our study also evaluates the capability of the ADCP in detecting methane bubble presence over the long term. Because ADCP detections rely on fixed geometry of the instrument's beams, the ADCP has limitations in detecting targets with motion such as the constantly floating methane bubbles that flow with the current. This limitation is exemplified by our observation such that bubble detections in ADCP are dependent on the local tidal current direction (Figure 8), as well as the prevailing background current (Figure 7). When the prevailing background current predominantly flowed NW with the tidal current fluctuating between N and NW, clear reductions were observed in our methane bubble detections (Figure 7). We believe that such reductions are caused by bubbles escaping from intersecting the ADCP beam. Therefore, to ensure the ADCP's performance in detecting methane bubbles, high probability of bubbles intersecting the ADCP beams is necessary. In our study, our confidence in the ADCP detections is enhanced by the fluctuating current direction at various tidal phases in which case time period with relatively uniform flow direction is eliminated in our analysis.

Although the ADCP has limitations in detecting bubbles, we believe that the instrument has demonstrated its reliability in detecting methane bubble presence from close-distance bubble sources over the long term. Particularly for the purpose of this study, we believe that the ADCP was able to capture most of the bubbles from Seep B and Einstein's Grotto which sit within a

100-m radius of the ADCP. Our confidence in the ADCP detection came from the $V_{bubble}$ to current speed ratio of 1.79 and bubble rising angles of smaller than 28.92°. With these bubble-rising behavior, close-distance bubbles would intersect the ADCP beam, if not at a shallow height, at a height in which the beams have wider widths where the current disperses the bubble plume laterally. In addition, our bubble rise height of ~400 m is similar to those imaged by high-resolution ship-based sonar in a previous study (Philip et al., 2018). With that, we argue that an ADCP is a useful instrument for studying methane bubble presence over the long term.

To maximize the application of an ADCP in detecting bubbles for future studies, the locations of bubble source, local current speed and direction, and the ADCP geometry should be evaluated pre-deployment. For example, deploying a standard current meter may allow greater accuracy of the bottom current speed and direction without the acoustic "noise" from bubbles. Assuming a bubble rising velocity greater than the current speed, an ADCP should be deployed such that the bubble rising angle approximates the ADCP beam angle with bubble source is within ~150-m proximity of the ADCP. In the case of bubbles escaping from the beam detection due to the limitation of an ADCP's geometry, deploying another ADCP with a geometry of opposite directions would allow detections of bubbles that escape from the first ADCP. Therefore, for future studies, having multiple ADCP's coupled with a more standard current meter that are judiciously placed would allow total detections of all relevant fluid flow with greater accuracy.

### 6.4 Implication for sensitivity of methane bubble emissions and future possibilities

Our result indicates that methane bubble emissions at SHR are sensitive to pressure change. Seafloor pressure change of ~3.3 dbar due to tides, equivalent to 0.4% of the overall water

thickness at SHR, had led to a magnitude change of ~2.5 times in the abundance of methane bubble plumes over 3.5 months (Figure 11). This sensitivity of bubble emissions suggests that the seafloor pressure decrease due to tides may have promoted the fracturing or reopening of the pre-existing fractures further allowing methane bubbles to escape into the ocean (Römer et al., 2016). Although previous study also suggested the potential of decreasing hydrostatic pressure due to tides in promoting the dissociation of methane hydrate at the base of MHSZ (Römer et al., 2016), validation of this mechanism requires our better understanding on the behavior of pore fluid pressure system and hydrate stability in response to hydrostatic pressure change.

To better understand the bubble emissions behavior at SHR, future studies with analyses on the relationship of temperature and earthquakes with bubble emissions are essential. In addition, a better understanding on the relationship between tides and pore fluid pressure system below the MHSZ, as well as hydrate stability, is necessary to understand the sensitivity of the seafloor hydrate system to pressure change. Study of such subtleties is possible through conducting a similar experiment with analyses of real-time data, transmitted via BluComm or Cabled Sensor array, from temperature probe, short-period seismometers and pore fluid pressure sensors (injected into the seafloor). Greater resolution of bubble emissions is likely attainable with the recently deployed underwater deep sea sonars at SHR (MARUM, 2018). In fact, pore fluid pressure sensors aside, the current cabled instrumentations at SHR includes broadband and short-period seismometers, benthic flow sensors, a mass spectrometer, a pressure sensor, a digital still camera, an Osmo fluid sampler, an ADCP, a current meter (Philip et al., 2016) and deep sea sonars (MARUM, 2018). By identifying a novel experimental configuration and taking advantage of the instrumentations at SHR, the possibilities exist for a comprehensive

understanding of hydrate (and bubble emissions) sensitivity to varying hydrostatic pressure, temperatures and earthquakes. Such comprehensive analyses may provide insights into the mechanisms controlling methane bubble emissions and hydrate stability.

## 7. CONCLUSION

Our study has demonstrated, with some limitations, how an upward-looking ADCP could be an adequate instrument for long-term studies of bubble emissions from seep sites. High-temporal resolution ADCP data reveals the significant tidal impacts on the frequency of methane emissions such that tides could modulate the frequency of methane emissions up to ~2.5 times over ~3.5 months. Because bubble presence was observed at all tidal phases throughout the study period, we propose a system of dynamic equilibrium between the seafloor pressure and the pore pressure for SHR. Although our study reveals how tides could modulate bubble emission behavior, future studies with analyses on the other parameters such as temperature, earthquakes and pore pressure are required to fully understand the hydrate sensitivity and bubble emissions behavior at SHR. Given that tides have significant impacts on the frequency of methane bubble emissions, tidal impacts should be considered in quantifying the amount of carbon or methane output from methane seeps.

## 8. REFERENCE


Archer, D. (2007). Methane hydrate stability and anthropogenic climate change. *Biogeosciences Discussions*, *4*(2), 993-1057.

Beaudoin, Y. C., Waite, W., Boswell, R., & Dallimore, S. R. (2014). *Frozen Heat: A UNEP Global Outlook on Methane Gas Hydrates.* Retrieved from http://wedocs.unep.org/bitstream/handle/20.500.11822/9357/GasHydrates_Vol2_screen.pdf?sequence=3&isAllowed=y

Bralower, T., & D. Bice (n.d.). Ancient Climate Events: Paleocene Eocene Thermal Maximum. Retrieved October 13, 2018, from https://www.e-education.psu.edu/earth103/node/639

Daigle, H., N. Bangs, & B. Dugan (2011). Transient hydraulic fracturing and gas release in methane hydrate settings: A case study from southern Hydrate Ridge. *Geochemistry, Geophysics, Geosystems, 12*(12), N/a, doi:10.1029/2011GC003841

Geologic History of Southern Hydrate Ridge. Retrieved July 13, 2018 from http://www-odp.tamu.edu/publications/204_SR/synth/synth_3.htm

Heeschen, K. U., Collier, R. W., de Angelis, M. A., Suess, E., Rehder, G., Linke, P., & Klinkhammer, G. P. (2005). Methane sources, distributions, and fluxes from cold vent sites at Hydrate Ridge, Cascadia Margin. *Global Biogeochemical Cycles*, *19*(2), doi: 10.1029/2004GB002266

Johnson, H., Miller, U., Salmi, M., & Solomon, E. (2015). Analysis of bubble plume distributions to evaluate methane hydrate decomposition on the continental slope. *Geochemistry, Geophysics, Geosystems,16*(11), 3825-3839, doi: 10.1002/2015GC005955

Katz, M. E., B. S. Cramer, G. S. Mountain, S. Katz, and K. G. Miller (2001). Uncorking the bottle: What triggered the Paleocene/Eocene thermal maximum methane release?, *Paleoceanography*, 16(6), 549–562, doi: 10.1029/2000PA000615.

Liu, L., Ryu, B., Sun, Z., Wu, N., Cao, H., Geng, W., Zhang, X., Jia, Y., Xu, C., Guo, L. & Wang, L. (2019). Monitoring and research on environmental impacts related to marine natural gas hydrates: Review and future perspective. *Journal of Natural Gas Science and Engineering*. 65, 82-107, doi: 10.1016/j.jngse.2019.02.007.

MARUM (2018, Jun 26). MARUM deep-sea sonars on Underwater Observatory. Retrieved Jun 1, 2019 from https://www.marum.de/en/Discover/MARUM-deep-sea-sonars-on-Underwater-Observatory.html

McGinnis, D., J. Greinert, Y. Artemov, S. Beaubien, & A. Wüest (2006). Fate of rising methane bubbles in stratified waters: How much methane reaches the atmosphere? *Journal of Geophysical Research: Oceans, 111*(C9), N/a, doi:10.1029/2005JC003183

OOI (2012, October 5). Data Product Specification for Velocity Profile and Echo Intensity. Retrieved April 21, 2019, from https://oceanobservatories.org/wp-content/uploads/2015/10/1341-00750_Data_Product_SPEC_VELPROF_ECHOINT_OOI.pdf

OOI (2018). OOI Data Portal. Retrieved Oct 1, 2018, from https://oceanobservatories.org/data-portal/

Philip, B., D. Kelley, E. Solomon, & J. Delaney (2016). Monitoring methane emissions at Southern Hydrate Ridge using an OOI Cabled Array Acoustic Doppler Current Profiler. *OCEANS 2016 MTS/IEEE Monterey,* 1-5.

Philip, B., A. Denny, E. Solomon, & D. Kelley (2016). Time−series measurements of bubble plume variability and water column methane distribution above Southern Hydrate Ridge, Oregon. *Geochemistry, Geophysics, Geosystems, 17*(3), 1182-1196, doi:10.1002/2016GC006250.

Rehder, G., Leifer, I., Brewer, P. G., Friederich, G., & Peltzer, E. T. (2009). Controls on methane bubble dissolution inside and outside the hydrate stability field from open ocean field experiments and numerical modeling. *Marine Chemistry*, *114*(1-2), 19-30, doi:10.1016/j.marchem.2009.03.004

Riedel M., M. Scherwath, M. Römer, M. Veloso, M. Heesemann, & G.D. Spence (2018). Distributed natural gas venting offshore along the Cascadia margin. *Nature Communications, 9*(1), 1-14, doi: 10.1038/s41467-018-05736-x

Römer M., M. Riedel, M. Scherwath, M. Heesemann, & G.D. Spence (2016). Tidally controlled gas bubble emissions: A comprehensive study using long−term monitoring data from the NEPTUNE cabled observatory offshore Vancouver Island. *Geochemistry, Geophysics, Geosystems, 17*(9), 3797-3814, doi: 10.1002/2016GC006528.

Ruppel, C. D. (2011). Methane Hydrates and Contemporary Climate Change. *Nature Education Knowledge* 3(10):29

Solomon, E., M. Kastner, H. Jannasch, G. Robertson, & Y. Weinstein (2008). Dynamic fluid flow and chemical fluxes associated with a seafloor gas hydrate deposit on the northern Gulf of Mexico slope. Earth and Planetary Science Letters, 270(1-2), 95-105, doi: 10.1016/j.epsl.2008.03.024

Torres, M. E., J. McManus, D. Hammond, M. A. d. Angelis, K. U. Heeschen, S. L. Colbert, M. D. Tryon, K. M. Brown, and E. Suess (2002), Fluid and chemical fluxes in and out of sediments hosting methane hydrate deposits on Hydrate Ridge, OR, I: Hydrological provinces, Earth Planet. Sci. Lett., 201, 525–540, doi: 10.1016/S0012-821X(02)00733-1

Tryon, M. D., K. M. Brown, M. E. Torres, A. M. Trehu, J. McManus, and R. W. Collier (1999), Measurements of transience and downward fluid flow near episodic methane gas vents, Hydrate Ridge, Cascadia, Geology, 27(12), 1075–1078, doi: 10.1130/0091-7613(1999)027%3C1075:MOTADF%3E2.3.CO;2

Wiggins, S.M, I. Leifer, P. Linke, & J.A. Hildebrand (2015). Long-term acoustic monitoring at North Sea well site 22/4b. *Marine and Petroleum Geology, 68*(PB), 776-788, doi: 10.1016/j.marpetgeo.2015.02.011

## 9. FIGURES

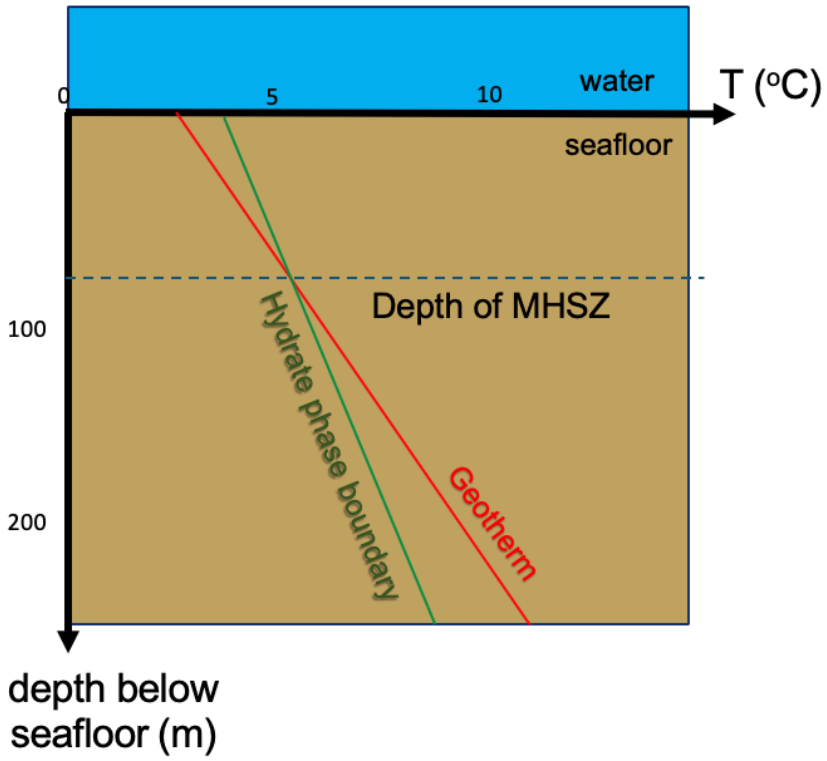


**Figure 1.** Thermodynamic conditions of the methane hydrate stability at the upper continental slope margin. Depth of MHSZ (brown dashed-line) is defined by the intersection between geotherm (red line) and hydrate phase boundary (green line). Above the MHSZ, methane exists within sediments in the form of hydrate. Below MHSZ, methane hydrate dissociates into fluid. Depth of MHSZ marks the lower limit of hydrate stability. Figure is recreated with reference to phase diagram of methane hydrate in Ruppel (2011).

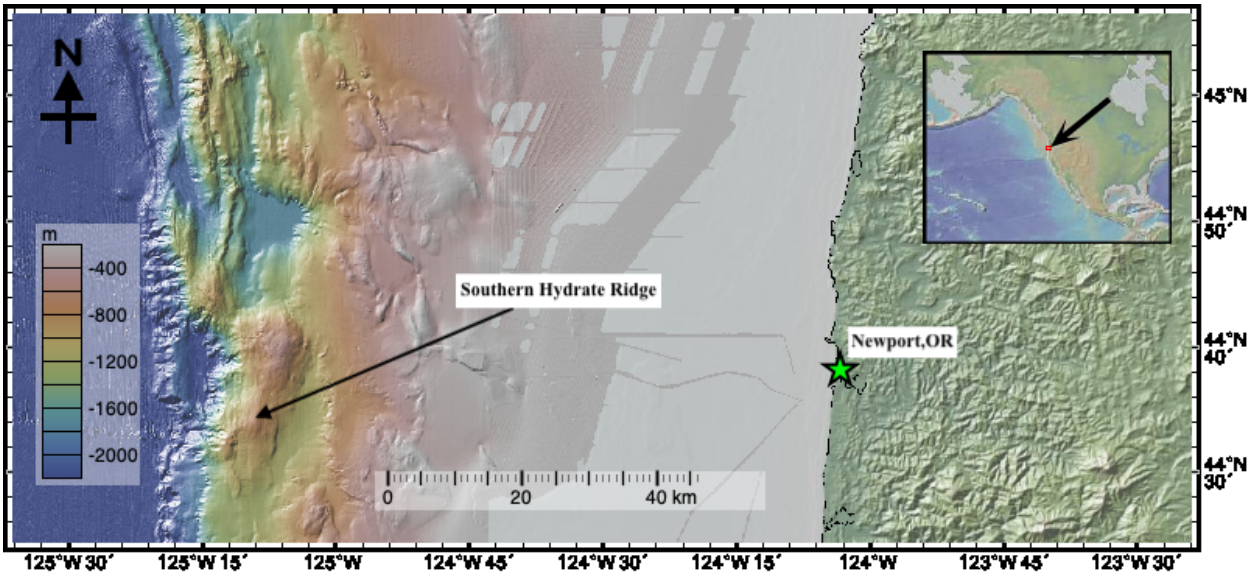


**Figure 2.** Location of SHR. Green star indicates the approximate location of Newport, Oregon. SHR is located on an upper continental slope margin.

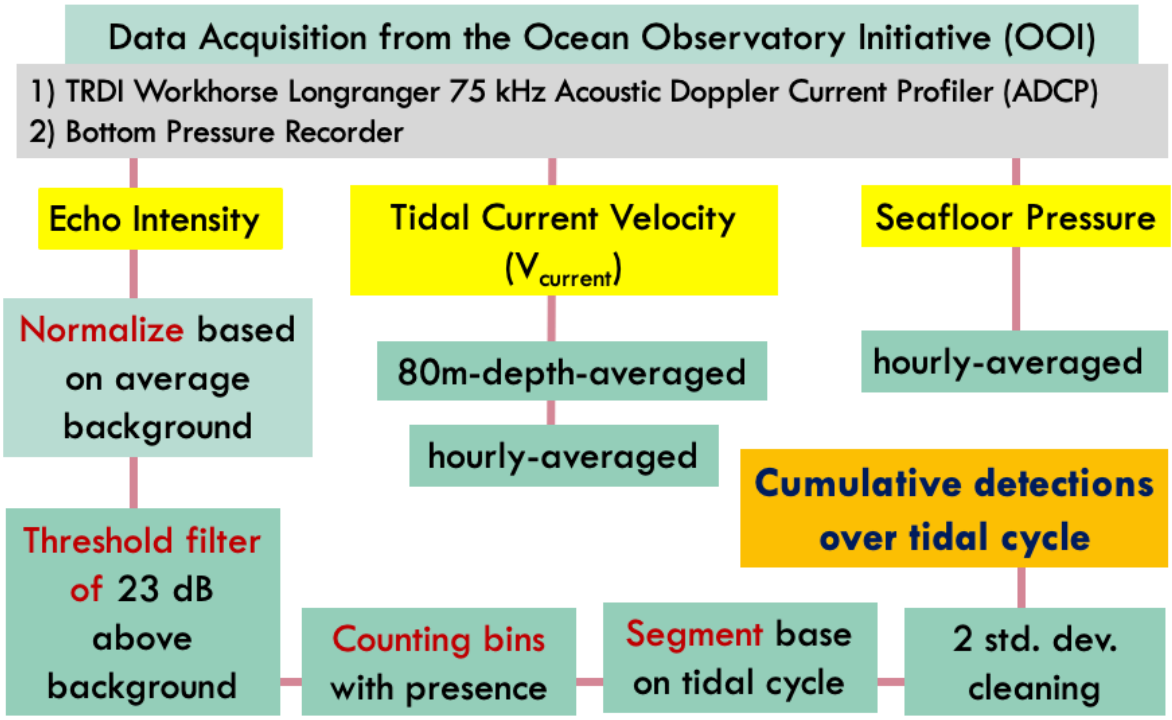


**Figure 3.** Data acquisition, processing and analysis workflow to obtain our result of cumulative detections over the tidal cycle.

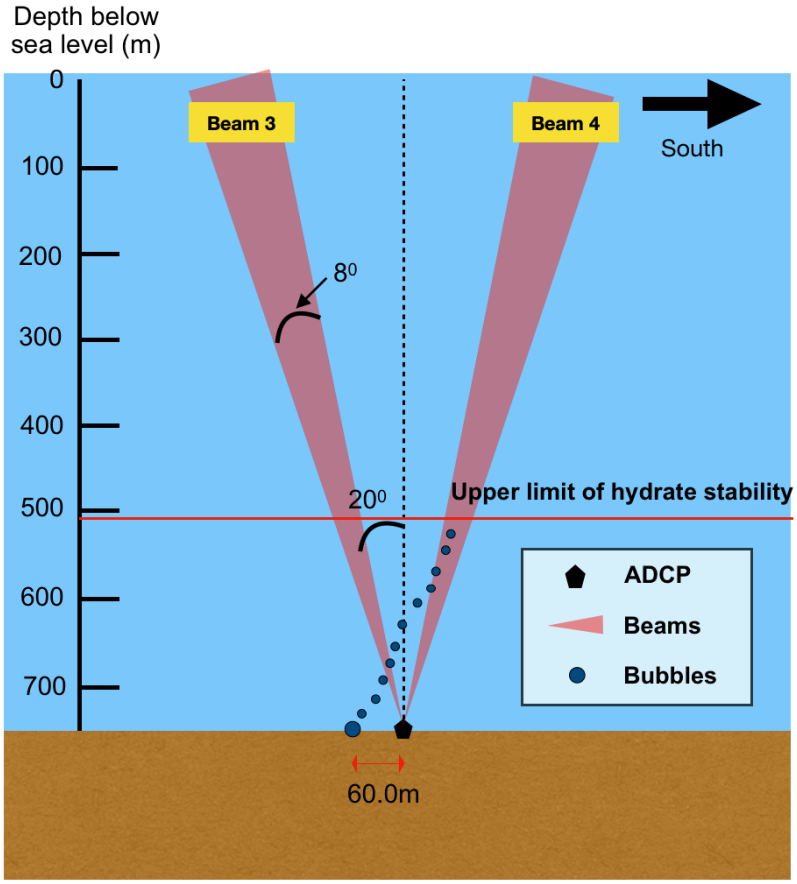


**Figure 4.** 2-D simulation of bubble transport into the ADCP beam along a N-S transect from a bubble source ~60 m north of the ADCP during a period with southward flowing current. Note that the beams of the ADCP are angled at 20$^{o}$ from vertical. Upper limit of hydrate stability is located ~510 m below sea level (Philip et al., 2016).

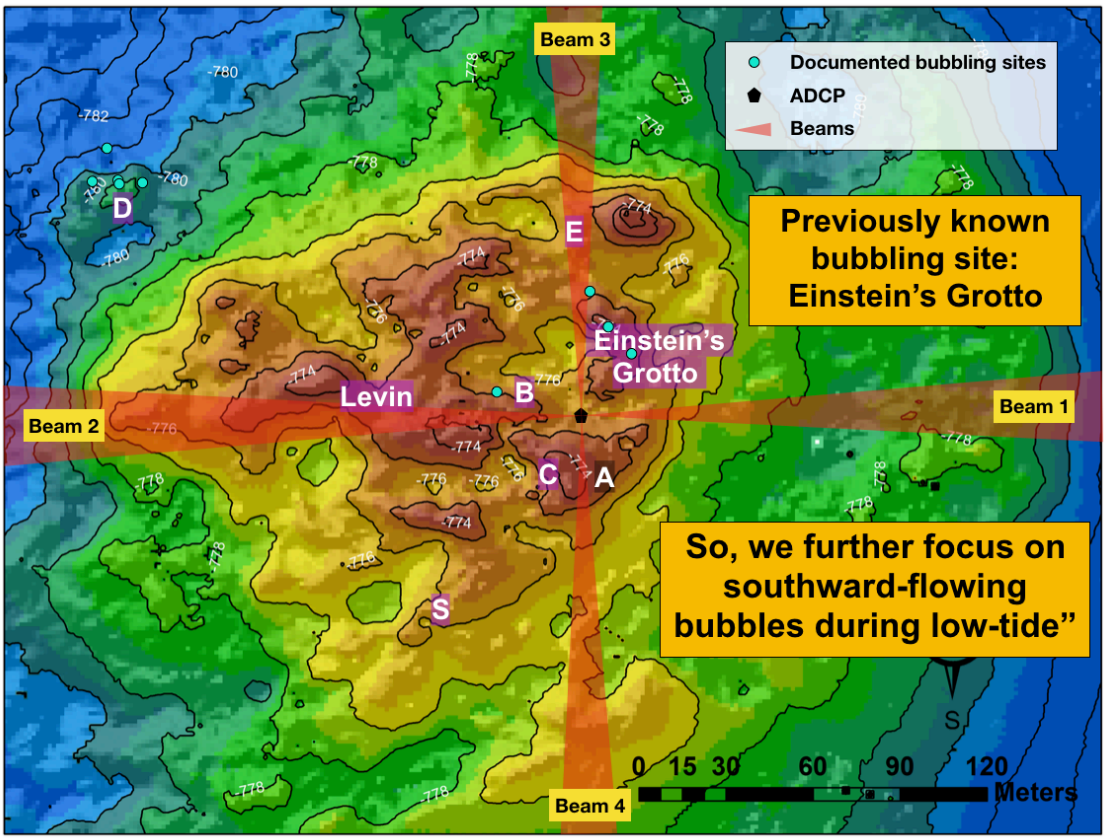


**Figure 5.** Bathymetry map of SHR annotated with ADCP beams' configuration. Bathymetric data were obtained during the 2010 Regional Cabled Array survey cruise at SHR using the autonomous underwater vehicle *Sentry* and R/V *Thompson* (courtesy of UW).

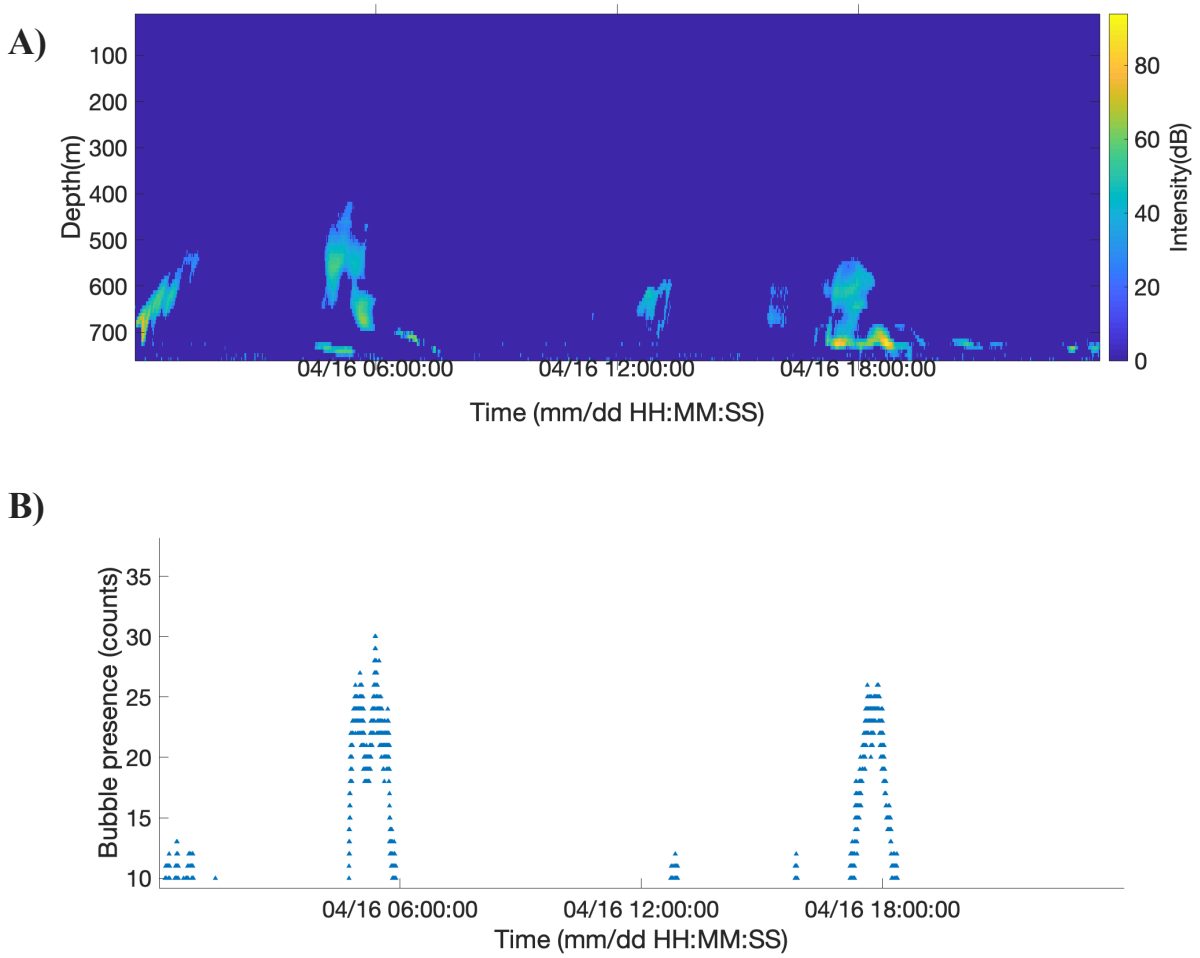


**Figure 6.** (A) One-day transect of processed echo intensity data showing bubble presence detected by Beam 3 on 4/16/2015. Bubble presence is depicted by the high intensity  Note the remaining random noise in the background. (B) Counts of bin cells containing bubble presence (after 2-standard-deviation cleaning) detected by Beam 3 on 4/16/2015.

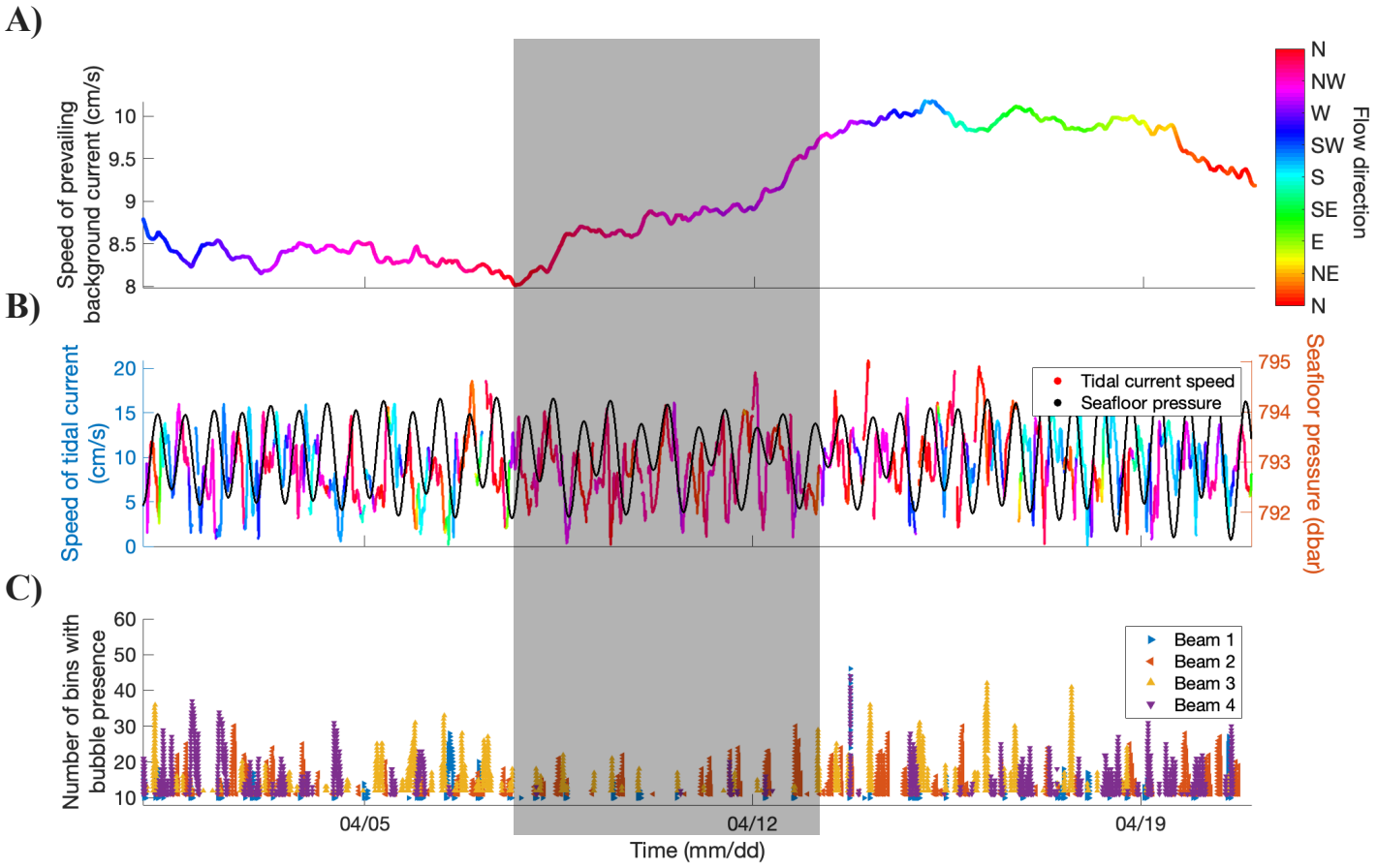


**Figure 7.** (A) The speed of prevailing background current from 4/1 to 4/20. Color indicates the current slow direction. (B) Seafloor pressure (black line) and the speed of tidal current (colored) from 4/1 to 4/20. Figure 7B shares the same color bar as in figure 7A. (C) Number of bin cells with methane bubble presence from all 4 beams. Orientation and color of markers indicate the source of detection described in the legend. Note the reductions in methane bubble detections during period with dominating NW flowing current highlighted by grey box. To avoid potential bias in our result (see discussion), this section of data is excluded from our analysis of cumulative detections over tidal cycle.

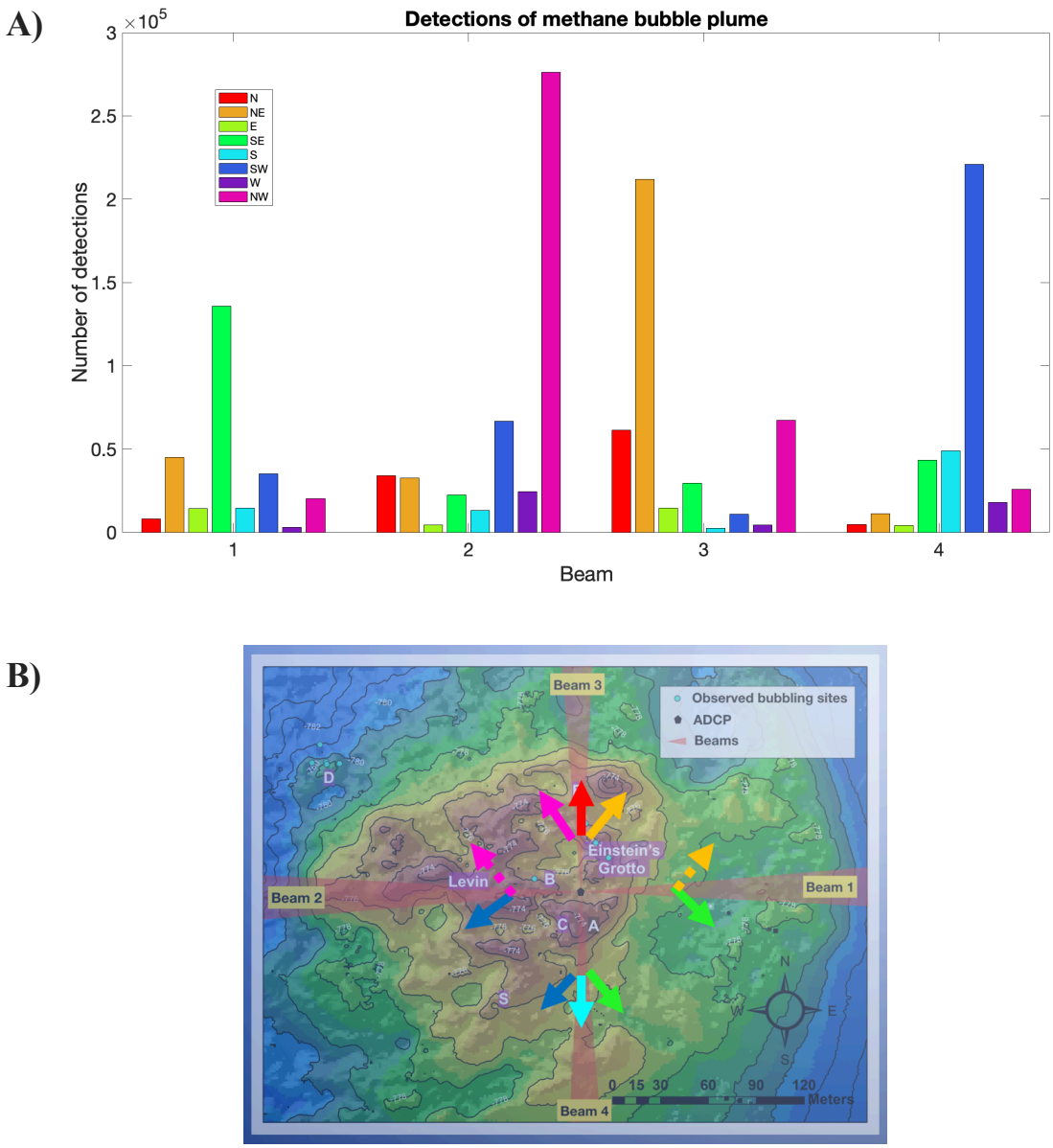


**Figure 8.** (A) Distribution of flow direction of methane detected bubbles in individual ADCP beam. (B) Plan view of the SHR annotated with predominant flow directions of detected bubbles in individual ADCP beam. Solid arrows indicate bubble flow directions away from Einstein's Grotto and Seep B. Dashed arrow indicates detections with bubble flow directions that are not parallel to direction away from any of the seep sites.

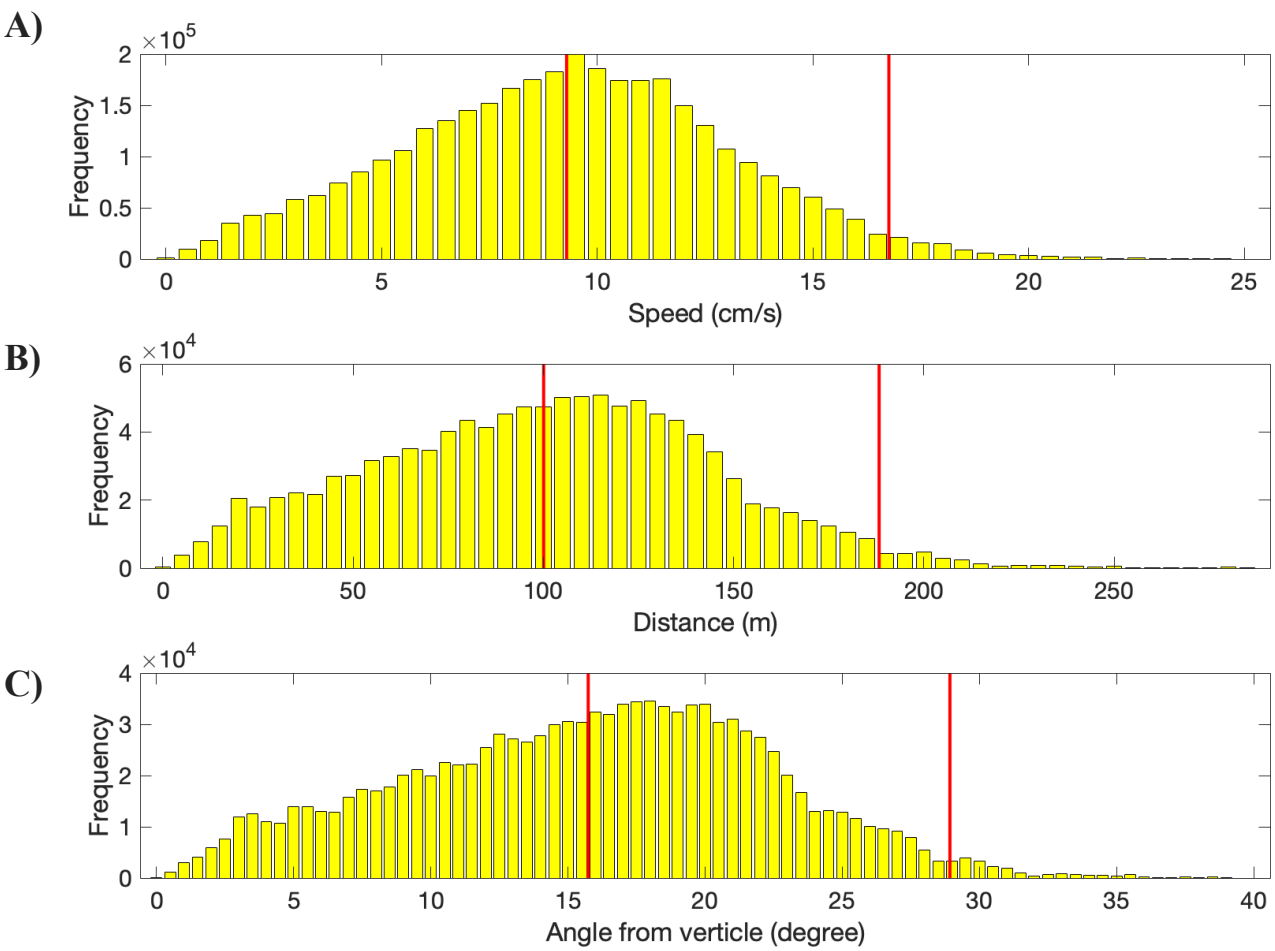


**Figure 9.** (A) Distribution of 80-m-hourly-averaged tidal current speed at SHR. (B) Distribution of potential maximum bubble source distance from the ADCP. (C) Distribution of bubble rising angles from vertical for the detected bubbles. In all plots, the first red vertical line indicates the mean value while the second indicates the upper bound value with 95% confidence level.

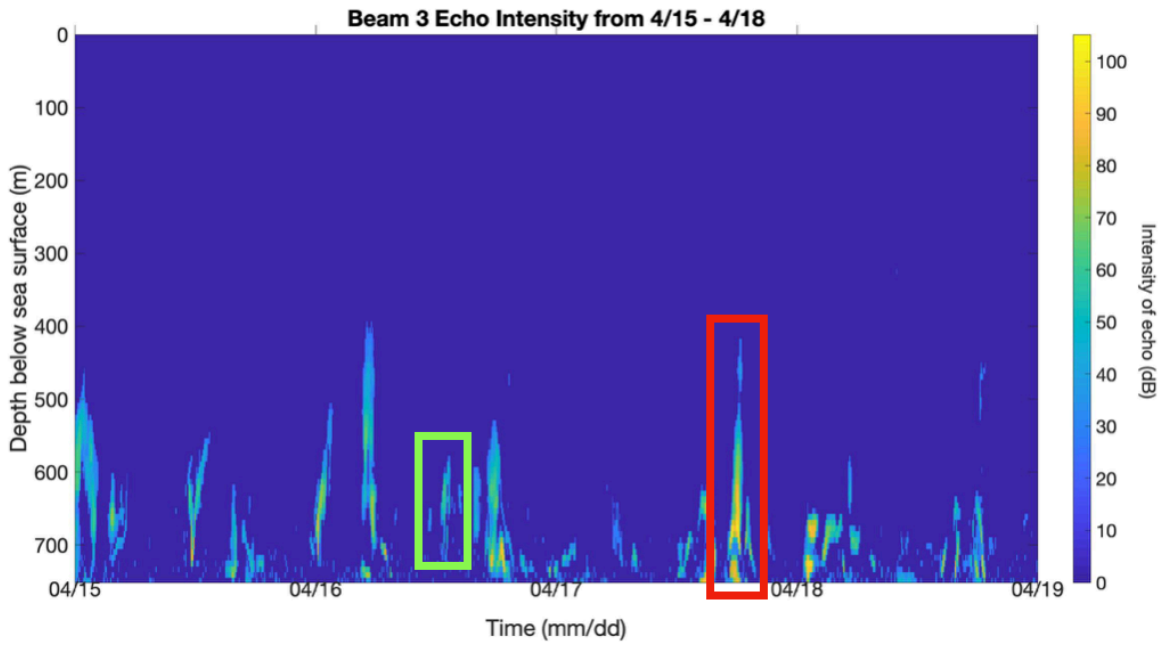


**Figure 10.** Transect of echo intensity showing bubble presence detected by Beam 3 from 4/15/2015 till 4/19/2015. Note the maximum height the plume rises above seafloor detected at depth ~400 m by the ADCP. The red box highlights a bubble plume detected starting from a low height. The green box highlights a bubble plume detected starting from a mid-height.

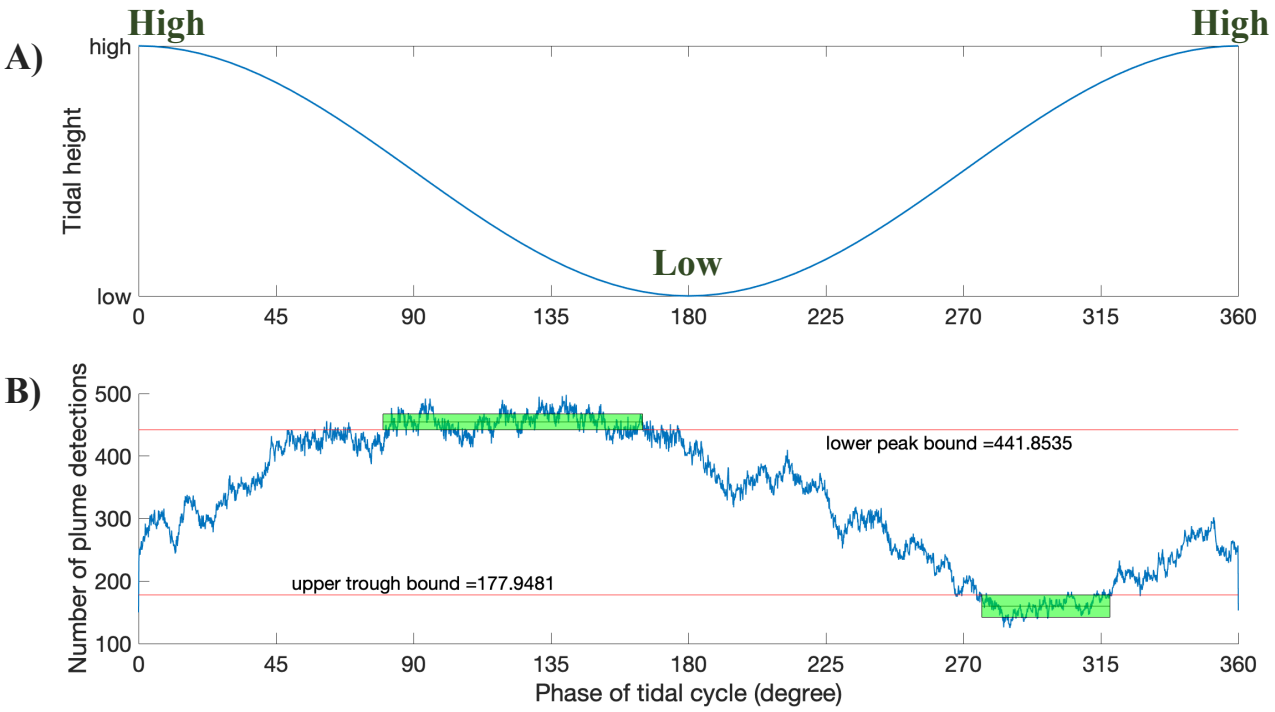


**Figure 11.** (A) Tidal cycle from high tide to high tide annotated by text in dark-green. (B) Cumulative bubble detections over the tidal cycle described in figure 11A. Green bars at the peak and the trough of the curve shows the confidence interval for mean value at respective phase. Note the sinusoidal behavior of the cumulative detection curve that lags ~120 degree from the tidal cycle curve.

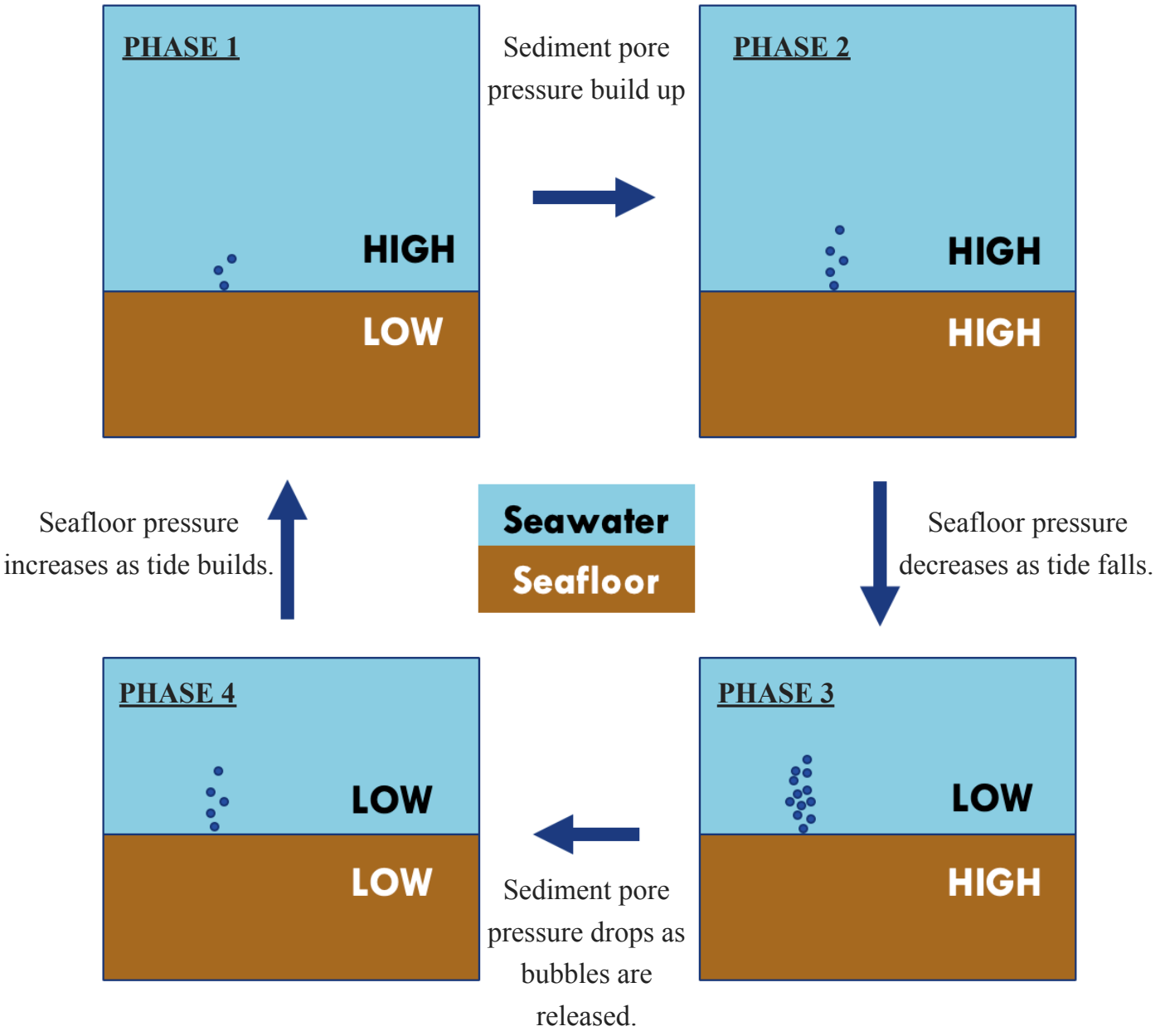


**Figure 12.** Schematic model of long-term bubble emission behavior at SHR. Density of bubbles indicate the relative tendency of bubble emissions. Black letters describe seafloor pressure and white letters describe the sediment pore pressure. Diagrams are not to scale.